Article

Cooling Improvement for High-Power-Density Shell-Mounted Underwater Propulsion Motors with Heat Bridges

Huanyu Ou [1,2], Yuli Hu [1,2], Zhaoyong Mao [1,2,*], Wenlong Tian [1,2] and Bo Cheng [1,2]

1   School of Marine Science and Technology, Northwestern Polytechnical University, Xi'an 710072, China; ouhuanyu@mail.nwpu.edu.cn (H.O.); zx670821@nwpu.edu.cn (Y.H.); tianwenlong@mail.nwpu.edu.cn (W.T.); chengbov@163.com (B.C.)
2   Key Laboratory for Unmanned Underwater Vehicle, Northwestern Polytechnical University, Xi'an 710072, China
*   Correspondence: maozhaoyong@nwpu.edu.cn

Abstract: Subject to an autonomous underwater vehicle (AUV) with rigorously limited space and weight, the high-power-density propulsion motor urgently needs an efficient cooling method to improve reliability and stability. In this paper, a cooling improvement method based on heat bridges (HBs) is proposed for the shell-mounted propulsion motor (SmPM) of the AUVs. First, the electromagnetic and thermal characteristics of a 150 kW SmPM are analyzed using a numerical method. Then, a prototype was developed and tested to verify the accuracy of the numerical calculation. Subsequently, in order to further improve the cooling performance of the motor with minimal weight increment, this paper proposes HBs mounted on the end winding. The maximum winding temperature of the motor containing the proposed HBs is decreased by 20 K at the rated operation state. Based on the validated numerical method, the effects of topologies, materials, and geometric parameters on the cooling effect are investigated. Furthermore, according to the required operating time, the SmPM is optimized based on the cooling performance improvement provided by the proposed HBs. The results show that in addition to the benefit of the cooling improvement contributed by the proposed HB, the weight of the propulsion motor is reduced by 7.14%.

Keywords: autonomous underwater vehicle (AUV); propulsion motor; cooling; heat bridge (HB)

1. Introduction

Due to its high efficiency, quietness, and superior control performance [1], the electric autonomous underwater vehicle (AUV) is becoming increasingly promising in marine technology applications, including marine exploration, rescue, and organism tracking [2,3]. As a propulsion motor, the permanent magnet synchronous motor (PMSM) is gaining attention in various types of AUVs due to is high efficiency, high-power-density, quietness, and excellent controllability [4,5].

Generally, AUVs sail underwater in a delicate balance between gravity and buoyancy [6]. At the same time, the propulsion motor must be mounted in the tail section to drive the propulsor. In order to achieve a satisfactory hydrodynamic performance, the tail section is usually designed to be streamlined. It results in the buoyancy of the tail section being slightly less than that of the head section. Consequently, strict requirements are imposed on the size and weight of the propulsion motor during the design process. Due to high electrical load and low thermal capacity, the high-power-density motor is known to have higher heat generation rates. On the other hand, the enclosed and compact interior space of the AUV provides a harsh thermal environment for the propulsion motor [7,8], making it susceptible to overheating. This will result in further increased losses and even deteriorations, such as the irreversible demagnetization of permanent magnets (PMs) and the dissolution of insulation. Therefore, an efficient cooling system is of paramount importance for the reliable operation of the high-power propulsion motor.

As a classic electrical system, the electric motor has already achieved a great deal of theoretical and applied research in heat dissipation technology [9,10]. According to the coolant medium, the common cooling technology of the motor can be divided into air cooling and liquid cooling [11].

Air cooling, including natural cooling and forced cooling, is usually used for relatively low-power-density motors. When air cooling is used for small or medium electric motors, fans are usually added inside the motor to force the air to flow for cooling. Chang et al. [12] investigated the cooling characteristics of fan-based electric motors for unmanned aerial vehicles (UAVs) based on a proposed comprehensive evaluation factor for cooling performance. It was shown that the cooling efficiency of the studied air-cooled motor increased by 27.78% as the fan speed increased from 800 rpm to 2000 rpm. In addition, when air cooling is used for high-power motors, they are usually equipped with a ventilation system. Xu et al. [13] proposed an air deflector for the ventilation system to enhance the cooling performance of a 600 kW axially forced air-cooled motor. The analysis using a numerical method shows that the optimized ring-type air deflector can significantly improve the cooling effect and pressure drop. In order to suppress the temperature rise of a 315 kW, 6 kV high-voltage line-started solid rotor permanent magnet synchronous motor (HVLSSR-PMSM), Li et al. [14] proposed an air-cooled hybrid ventilation system. Theoretical and experimental studies have shown a significant decrease in the maximum rotor temperature, thus improving the stability and reliability of the motor operation. However, the confined space and very small amount of air inside the AUV make it almost impossible to apply air cooling to the propulsion motor of the AUV for heat dissipation.

Compared to air cooling, liquid cooling offers better cooling performance and more potential applications. Liquid cooling, such as water jacket cooling (WJC) [15], oil spray cooling [16,17], and mixed liquid cooling, cools the motor through convective heat transfer between the highly thermal-conductive coolant medium and hot components. Lee et. al. [18] proposed a U-shaped water jacket design with guide vanes for in-wheel motors (IWMs). The multi-objective optimization of the U-shaped water jacket was implemented, and an effective reduction of both the maximum winding temperature and the pressure drop was achieved. However, it is difficult to cool the motor end windings effectively with WJC. Park et. al. [19] carried out a comparative study of a direct slot cooling motor (DSC) and a water jacket cooling motor. The results showed that the DSC motor exhibited thermal durability at a current density 80% higher than that in the WJC motor under the same coolant pumping power.

Although water has high liquidity and specific heat, its tendency to oxidize silicon steel sheets and PMs means that injecting it into the motor for direct cooling risks damaging the motor. In contrast, oil spray cooling cools by spraying oil directly onto hot spots, which not only provides more efficient cooling but also does not damage electromagnetic components [20]. In order to improve the cooling of commercial electric driving motors, Garud et al. [21] proposed a novel multi-nozzle-based oil spray cooling. Based on a coupled numerical analysis, the effects of the nozzle locations, cooling oil types, flow rates, and oil inlet temperature on the cooling effect were investigated. The proposed multi-nozzle-based oil spray cooling technique can be effectively applied to commercial electric driving motors of any configuration. Wang et al. [22] proposed a novel hollow shaft oil injection cooling structure to suppress the internal temperature of the motor. The effect of the proposed oil spray cooling structure on the average winding temperature was analyzed using Taguchi's method, which provides an optimized solution with a smaller flow difference. As a closed-cycle cooling system, oil spray cooling, like water jacket cooling, requires not only auxiliary equipment such as pumps, piping, heat exchangers, and reservoirs but also the sealing of the coolant circuit to prevent leakage.

In summary, all the above methods are effective in suppressing the temperature rise for the electric motor, but the extra equipment required increases the cost and complexity of the system. In this paper, a 150 kW shell-mounted propulsion motor (SmPM) for AUVs is numerically analyzed and experimentally investigated. First, the electromagnetic and

thermal characteristics are calculated using the numerical method. Then, a prototype is developed and tested to verify the accuracy of the numerical prediction. Subsequently, in order to further improve the cooling performance of the motor with minimal weight increment, this paper proposes HBs mounted on the end winding. Based on the validated numerical method, the effects of topologies, materials, and geometric parameters on the cooling effect are investigated. Furthermore, according to the required operating time, the SmPM is optimized based on the cooling performance improvement provided by the proposed HBs.

2. Prototype and Methodology

2.1. Prototype Description

The propulsion motor represents a pivotal component within the power system of the AUV. It consumes electrical energy stored in the battery and converts it into mechanical energy to propel the AUV. Most conventional motor cooling methods require additional auxiliary equipment, such as a coolant medium, heat exchanger, and pump inside or at the periphery of the motor, which not only increases the size and space occupation but also increases the manufacturing cost and the complexity.

In order to fully utilize the seawater outside the AUV shell for effective cooling, this paper demonstrates a cooling scheme, as shown in Figure 1. In the proposed cooling solution, the stator and rotor are mounted directly inside the aluminum alloy AUV shell, eliminating the shell of the generic motor. Furthermore, the aluminum alloy's efficient heat transfer behavior enables the rapid dissipation of electromagnetic losses generated inside the stator windings into the cold seawater, thus removing the coolant medium or the auxiliary equipment for the propulsion motor. Benefitting from differing speeds of the AUV, the SmPm is also capable of regulating cooling in the absence of a control system. That is, when the SmPm is operating at a higher power, a greater quantity of waste heat is generated. Simultaneously, benefitting from the stronger cooling capacity contributed by the higher AUV speed, the motor can be guaranteed to operate within a safe temperature range.
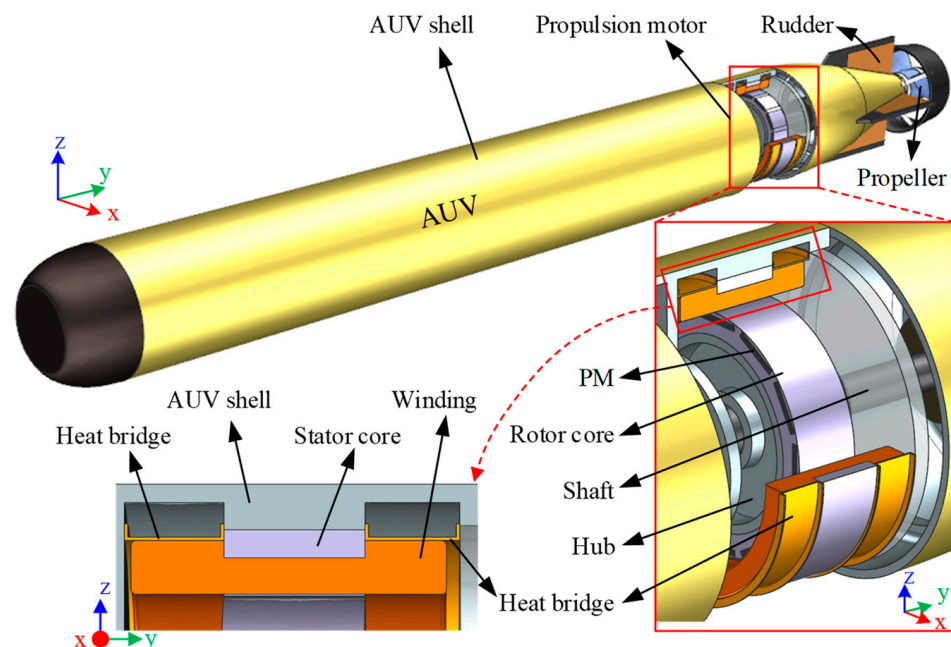
Figure 1. Cooling scheme for the AUV propulsion motors.

It is always a concern that due to the end winding being wrapped in the air within the motor, a localized hot spot may appear at the end winding. In order to ensure that the end winding is cooled by seawater simultaneously, this paper proposes the HBs, which consist of a highly thermally conductive metallic material. Prior to the installation of the HBs, the

end winding should be pressed flat by a mold, and the HBs should be manufactured in a specific shape to fit over the end winding. This creates an efficient thermal path between the end windings and the cold AUV shell, thereby ensuring optimal heat transfer. Thermally conductive silicone grease is applied between the HBs and the end winding to enhance the thermal contact conductance.

In this paper, a 6 min-operated PMSM with an interior permanent magnet rotor is investigated. The relevant parameters are presented in Table 1. A 12-pole, 72-slot scheme is adopted for the studied PMSM, which has a distributed winding with 3 parallel branches. It is pertinent to note that when the motor operates at the rated rate, the studied AUV is derived underwater for a duration of 6 min at a velocity of 21.5 m/s.

Table 1. Relevant parameters of the PMSM.

Parameter	Value	Parameter	Value
Rated power [kW]	150	Rated speed [rpm]	2600
Slots	72	Pole pairs	6
Stator inner diameter [mm]	315	Stator outer diameter [mm]	395
Stator length [mm]	82	Rotor inner diameter [mm]	250
Air gap [mm]	2	Magnet thickness [mm]	8
Pole-arc coefficient	0.833	Turns	4
Winding pitch	5	Parallel branches	3

2.2. Mathematical Model

2.2.1. Heat Generation

In order to simplify the calculation model, this paper postulates that the losses inside each electromagnetic component of the motor are uniformly distributed. Consequently, the heat generation rate of one component can be expressed as follows:

$$h_g = \frac{P_l}{V_p} \tag{1}$$

where P_l is the average power loss of the component. V_p is the volume of the component.

In general, the losses of PMSM are primarily comprised of three parts, including copper losses in the windings, iron losses in the iron core, and eddy current losses in the permanent magnets (PMs) [23]. For the integer slot scheme studied in this paper, the relative lack of high harmonic content in the magnetic field results in a relatively small amount of losses in the rotor [24], with copper losses and stator iron losses accounting for the majority of the losses.

A.   Copper loss

Copper loss is typically composed of DC loss and additional AC loss caused by the skin effect and proximity effect when the winding is fed with an AC current [25]. With the exception of DC loss, the additional AC loss is closely related to the frequency of the fed AC current. In this paper, the winding of the investigated SmPM is composed of multi-stranded wire, with a small wire diameter (1.25 mm). Furthermore, the AC current frequency corresponding to the maximum speed of the motor studied is 260 Hz, which is far from exceeding 2.5 kHz. Therefore, the additional AC loss in the PMSM can be disregarded [26]. In this instance, it can be postulated that copper loss remains constant with respect to speed. Consequently, the relationships between winding copper loss and current can be expressed as follows:

$$P_{Cu} = 3I_{ph}{}^2 R_{ph} = 3I_{ph}{}^2 \frac{N_c N_t}{N_p N_s} \frac{\rho_c l_c}{A_c} \tag{2}$$

where R_{ph} represents the phase resistance. The number of turns of the coil is N_c. ρ_c is the resistivity of the copper wire at actual temperature, and l_c is the average length of a single-turn coil.

B.   Iron loss

The iron loss in the stator core stack is comprised of hysteresis loss, eddy current loss, and additional loss [27]. The complexity of the factors, such as the loss composition mechanism, inhomogeneous magnetic field, and manufacturing technology, present a significant challenge in calculating the iron loss accurately [28]. According to the iron loss separation model proposed by Bertotti [29], it is considered that under an alternating magnetic field, there is rotational magnetization and alternating magnetization inside the silicon steel sheet, both of which generate losses [30]. Considering the significant differences in magnetic field characteristics and strength between stator yoke and tooth, whose iron loss calculation is separated in the paper to improve the accuracy of temperature field prediction. The iron loss can be expressed as follows:

$$
P_{iron} = P_{iron\_y} + P_{iron\_t} = \iiint\limits_{yoke} \left[k_h f B_{py}^\beta + k_c \left(\frac{dB_y(t)}{dt} \right)^2 + k_e \left(\frac{dB_y(t)}{dt} \right)^{1.5} \right] dV
$$
$$
+ \iiint\limits_{teeth} \left[k_h f B_{pt}^\beta + k_c \left(\frac{dB_t(t)}{dt} \right)^2 + k_e \left(\frac{dB_t(t)}{dt} \right)^{1.5} \right] dV \tag{3}
$$

where k_h, k_c, and k_e are the coefficients of the hysteresis loss, eddy current loss, and additional loss, respectively. Assuming that there are no minor loops present in the hysteresis loop, the hysteresis loss depends on the peak of the magnetic flux density only [31]. B_{py} and B_{py} are the peaks of magnetic flux density on the hysteresis loop inside the yoke and tooth, respectively. β is the Steinmetz coefficient. $B_y(t)$ and $B_t(t)$ are the magnetic flux density in harmonic components of the yoke and tooth zoom, respectively.

C.   Eddy current loss

The eddy current loss in the rotor is generated by the high-order space-time harmonic magnetomotive forces (MMFs) of the motor. The eddy current loss of the rotor in a PMSM can be written as follows [32]:

$$
P_{EC} = \sum_v \int\limits_{PM} \frac{J_v^2}{2\sigma} dV \tag{4}
$$

where v is the harmonic order of the armature reaction magnetic field and σ is the conductivity of PMs. J_v is the eddy current density amplitude of vth-order harmonic and can be obtained from the induced eddy current density function, as follows:

$$
J = \sum_v J_v \cos(v\theta + p\Omega t + \alpha_v) \tag{5}
$$

where θ is the rotor angular position; p is the pole pairs of the rotor; Ω is the mechanical angular speed; t is the time; and α_v is the phase angle of vth-order harmonic.

2.2.2. Physics Field Model

Seawater outside the AUV shell and components of the SmPM are considered in the computational domain. In order to predict the characteristics of the temperature field of the SmPM, it is necessary to describe the flow and thermal phenomena in the system accurately.

Ideal air was assumed inside the motor for this study [16]. The governing equations are the turbulent model in this study [33] and are described as follows:

Turbulent kinetic energy is as follows:

$$
\frac{\partial}{\partial t}(\rho k) + \frac{\partial}{\partial x_i}(\rho k u_i) = \frac{\partial}{\partial x_j}\left(\Gamma_k \frac{\partial k}{\partial x_j} \right) + G_K - Y_K + S_K \tag{6}
$$

The specific dissipation rate is as follows:

$$\frac{\partial}{\partial t}(\rho\omega) + \frac{\partial}{\partial x_i}(\rho\omega u_i) = \frac{\partial}{\partial x_j}\left(\Gamma_\omega \frac{\partial\omega}{\partial x_j}\right) + G_k - Y_\omega + S_\omega \tag{7}$$

where, k is the feature speed of turbulence kinetic energy; G_K and G_ω are the turbulence kinetic energy production items; Γ_K and Γ_ω are the diffusion rate of the k and ω; Y_K and Y_ω are the turbulence dissipative items; S_K and S_ω are the source items. In addition, flows in the computational domain are governed by the laws of mass conservation and momentum [34].

The laws of mass conservation are as follows:

$$\frac{\partial\rho}{\partial t} + \frac{\partial(\rho\mathbf{u})}{\partial x} + \frac{\partial(\rho\mathbf{v})}{\partial y} + \frac{\partial(\rho\mathbf{w})}{\partial z} = 0 \tag{8}$$

The laws of momentum conservation are as follows:

$$\begin{cases} \frac{\partial(\rho\mathbf{u})}{\partial t} + \mathrm{div}(\rho u u) = -\frac{\partial p}{\partial x} + \frac{\partial\tau_{xx}}{\partial x} + \frac{\partial\tau_{yx}}{\partial y} + \frac{\partial\tau_{zx}}{\partial z} + F_x \\ \frac{\partial(\rho\mathbf{v})}{\partial t} + \mathrm{div}(\rho v u) = -\frac{\partial p}{\partial y} + \frac{\partial\tau_{xy}}{\partial x} + \frac{\partial\tau_{yy}}{\partial y} + \frac{\partial\tau_{zy}}{\partial z} + F_y \\ \frac{\partial(\rho\mathbf{w})}{\partial t} + \mathrm{div}(\rho w u) = -\frac{\partial p}{\partial z} + \frac{\partial\tau_{xz}}{\partial x} + \frac{\partial\tau_{yz}}{\partial y} + \frac{\partial\tau_{zz}}{\partial z} + F_z \end{cases} \tag{9}$$

where, i is the coordinate direction; F_i is the volume force on the micro-element; p is the static pressure on the fluid micro-element; and τ_{xx}, τ_{xy}, and τ_{xz} are the viscous stress components on the micro-element surface.

In thermodynamics, the stator core, winding, PMs, rotor core, and bearings generate heat owing to electromagnetic or mechanical losses. Then, the losses make the components of the PMSM to heat up, and dissipate through conduction, convection, and radiation. In this paper, the thermal radiation was disregarded. Thus, the heat transfer process satisfied the law of energy conservation as follows [35]:

$$\frac{\partial}{\partial t}(\rho T) + \mathrm{div}(\rho\mathbf{u}T) = \mathrm{div}(\frac{k_{ht}}{C_P}\mathrm{grad}\, T) + S_T \tag{10}$$

where, c_p is the specific heat capacity, T is the temperature of the fluid, k_{ht} is the fluid heat transfer coefficient, and S_T represents the heat source.

2.3. Numerical Method

2.3.1. Electromagnetic Performance

The accuracy of the electromagnetic field calculations directly affects the heat generation rate and the accuracy of the temperature prediction. In this paper, the finite element method (FEM) is used to predict the electromagnetic performance of the interior-rotor PMSM studied.

A 2D model with one pair of poles was employed to investigate the electromagnetic field in both no-loaded and on-loaded states, and the results are presented in Figure 2. The 3-phase currents with an advanced angle of 32 degrees, shown as Equation (11), are fed into the windings, and the magnetic field distribution is shown in Figure 2b. The results indicate that the magnetic flux density in the middle of the stator teeth in the absence of load is approximately 1.3 T. The magnetizing effect of the stator current results in a maximum magnetic density of the motor under a load of 1.8 T, which is close to the saturation limitation of the silicon steel sheet. The radial and tangential flux density components in the air gap and in the middle of the tooth under no-load and on-load states are decomposed and shown in Figure 3. The combined effect of the magnetic field excited by the PMs and the stator current results in a strengthened advancement of the radial fundamental wave of the load magnetic field, which drives the rotor to rotate. Nevertheless, in the loaded state,

an increase in tangential magnetic flux density is observed, which concomitantly results in an augmentation of iron core loss.

$$\begin{cases} i_a = \sqrt{2}I_m \sin\left(2\pi f \cdot t + \frac{32\pi}{180}\right) \\ i_b = \sqrt{2}I_m \sin\left(2\pi f \cdot t + \frac{32\pi}{180} - \frac{2\pi}{3}\right) \\ i_c = \sqrt{2}I_m \sin\left(2\pi f \cdot t + \frac{32\pi}{180} - \frac{4\pi}{3}\right) \end{cases} \tag{11}$$
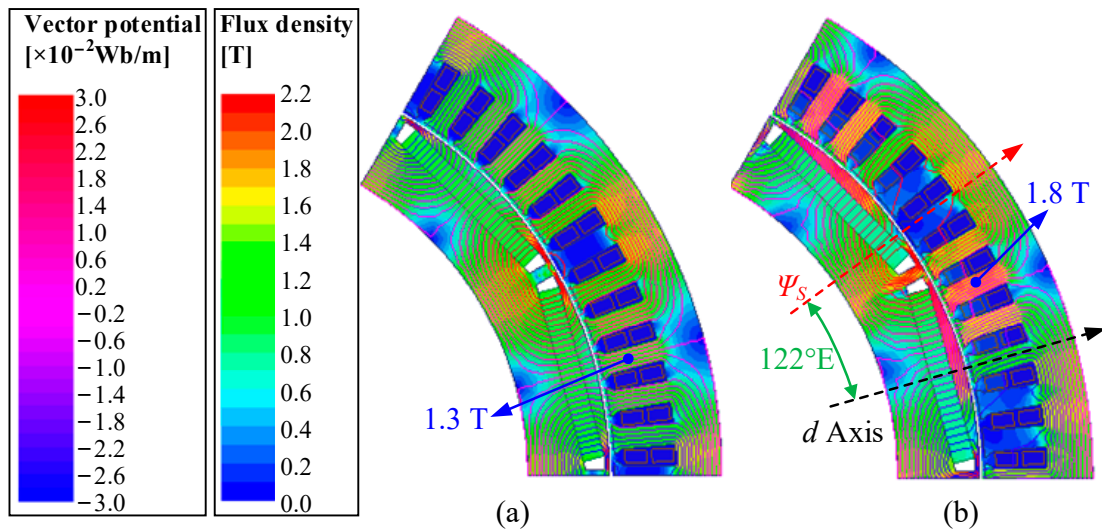

Figure 2. The electromagnetic field of the PMSM: (**a**) no-loaded; (**b**) 150 kW on-loaded.
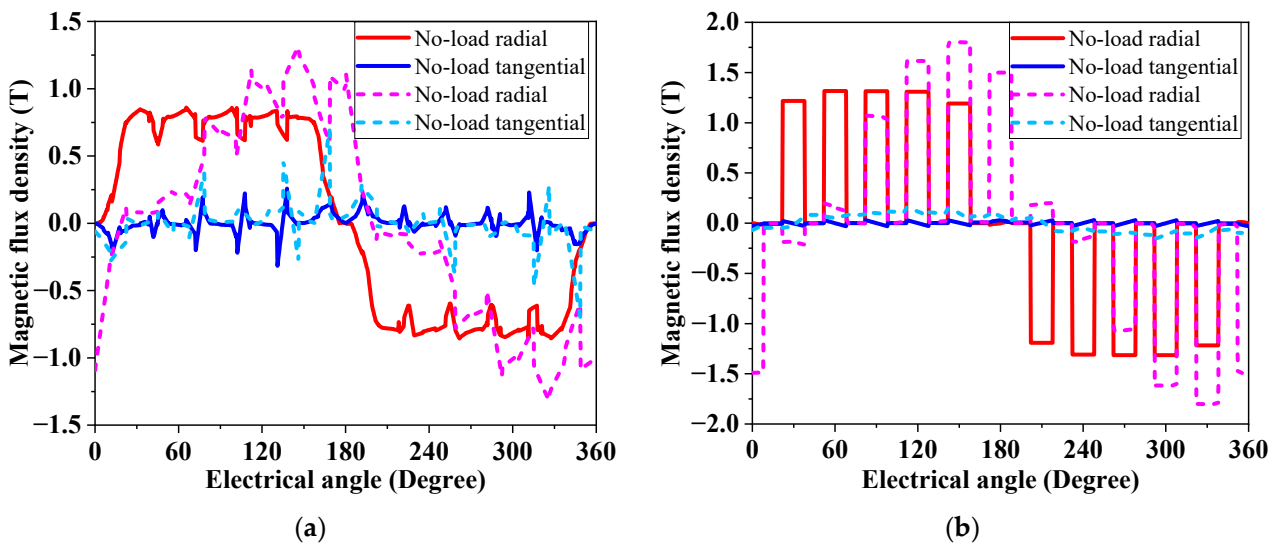
Figure 3. Flux density distributions at the (**a**) air gap and (**b**) tooth.

Figure 4 illustrates the line back electromotive force (back-EMF) of the motor in a no-load state with a speed of 2500 rpm. The results demonstrate that the amplitude of the back electromotive force of the no-load line is approximately 324 V. The total harmonic distortion (THD) of the line back-EMF is approximately 4.38%, indicating that the line back-EMF is highly consistent with the sine wave.
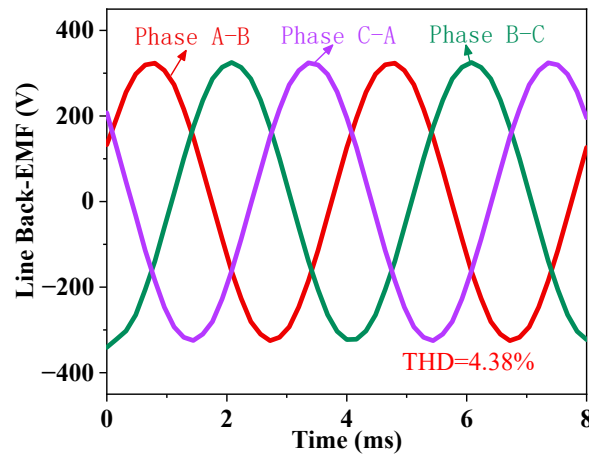
Figure 4. Line back-EMF at no-loaded state.

2.3.2. Temperature Prediction

Although the stator is shell-mounted inside the AUV and cooled by the seawater flowing at high speed outside, the temperature inside the high-power-density motor will still rise rapidly due to the large losses generated, resulting in a high risk of damage to the motor. Consequently, it is imperative to accurately predict the transient temperature rise of motors during high-power operation.

A.   Computational domain

In this paper, a section of the AUV containing the studied PMSM inside and seawater outside is used for transient temperature rise prediction, as shown in Figure 5. Based on the analysis of the iron core losses above, the yoke and tooth of the stator are modeled separately to improve the accuracy of temperature prediction. Furthermore, considering the intricate nature of the windings, an equivalent winding is employed, and the wedges are modeled separately in this paper.
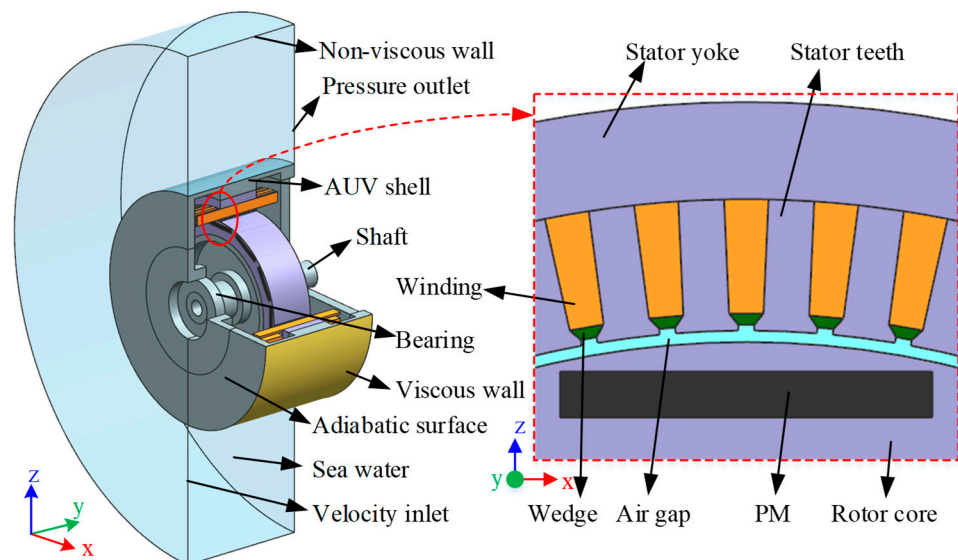

Figure 5. Computational domain models for temperature prediction.

B.   Heat generation

According to the output power of the propulsion motor corresponding to the different speeds of the AUV, the losses of each heating component are first calculated using the FEM, then the heat generation is calculated using Equation (1) and listed in Table 2. The output

power of the propulsion motor is approximately 120 kW and 150 kW at speeds of 20 m/s and 21.5 m/s, respectively. The heat generations at different output powers indicate that the primary losses of the propulsion motor during high-speed navigation of the AUV are copper and stator iron losses, while rotor iron loss and PM eddy current loss account for a relatively minor proportion. Therefore, this paper focuses on the transient temperature rise of the windings of the motor.

Table 2. Heat generations at different output power states.

AUV. Speed [m/s]	Output Power [kW]	Volumetric Heat Generation Rate [W/m^3]					
		Bearing	**PMs**	**Stator Yoke**	**Stator Tooth**	**Winding**	**Rotor Core**
21.5	150	272,351.6	4977.4	177,334.2	243,037.7	3,027,065.5	13,220.0
20	120	224,690.0	2884.6	190,271.5	227,563.1	1,937,300.5	11,646.6

C.   Boundary condition

In the studied situation, the SmPM propels the AUV to travel at high speeds underwater, but at the same time, it produces a certain amount of loss, causing the internal temperature of the SmPM to rise rapidly. Beneficially, the seawater that flows at a high speed on the external surface of the AUV provides favorable conditions for cooling the SmPM.

The physical and thermal properties of the components are listed in Table 3. The actual winding is constructed from multiple strands of enamel-covered wire and fixed in the stator slot by potting. It is challenging to model the winding accurately because the thermal characteristics of the winding are affected by many factors, such as slot fullness, winding form, and manufacturing process [36]. A significant number of studies have been conducted to investigate the equivalent model of the winding, which has been proven to predict the winding temperature accurately [37]. The thermal conductivity of the equivalent winding can be expressed as follows [38]:

$$
\begin{aligned}
&\text{Axial}: \ k_{w-A} = k_{cu}F + k_{im}(1-F) \\
&\text{Radial/Tangential}: k_{w-RT} = k_{im}\frac{(1+F)k_{cu}+(1-F)k_{im}}{(1-F)k_{cu}+(1+F)k_{im}}
\end{aligned}
\tag{12}
$$

where F is the slot full rate of the winding; and k_{cu} and k_{im} are the thermal conductivities of copper (388 W/m/K) and insulation (0.7 W/m/K), respectively.

Table 3. Physical and thermal properties of the components.

Components	Material	Density [kg/m^3]	Specific Heat [J/(kg·K)]	Thermal Conductivity [W/(m·K)]
AUV shell; Endcaps	Aluminum alloy	2790	924	193
Wedges	Epoxy	1200	1500	0.22
Magnet	NdFeB	7500	460	7.6
Shaft; Bearing	Steel	8030	502.48	16.27
Winding	Multi-stranded wire	5080	521.1	192.7 (Axial) 2.07 (Radial/Tangential)
Stator core; Rotor core	Silicon steel sheet	7800	460	3.86 (Axial) 28.51 (Radial/Tangential)

Generally, the stator core and rotor core of an interior PMSM are laminated and bonded by hundreds of silicon steel sheets. Thus, the axial thermal resistance can be equivalent to multiple thermal resistances connected in series, while the radial and tangential thermal

resistances can be regarded as multiple thermal resistances connected in parallel [39]. Then, the thermal conductivity of the laminated core is written as follows:

$$
\begin{aligned}
&\text{Axial}: k_{S-A} = k_S k_{Fe} + (1 - k_S)k_{in} \\
&\text{Radial/Tangential}: k_{S-RT} = \frac{k_{Fe}k_{in}}{kk_{in}+(1-k_S)k_{Fe}}
\end{aligned}
\tag{13}
$$

where k_S denotes the stacking coefficient; and k_{Fe} and k_{in} are the thermal conductivities of the silicon steel (30 W/m/K) and the insulation (0.22 W/m/K), respectively.

The computational domain of the propulsion motor depicted in Figure 5 was employed to predict the thermal and flow characteristics utilizing ANSYS FLUENT software (Version 17.0). The boundary conditions used in this study are marked in Figure 5. Seawater with a temperature of 300 K flows into the computational domain at the velocity inlet with the navigation speed of the AUV, cooling the propulsion motor and subsequently flowing out at the zero-pressure outlet. Furthermore, the Dirichlet and Neumann boundary conditions are employed at the solid–fluid interfaces, and the non-viscous boundary is used at the exterior surface of the seawater domain [32]. Considering the limited contribution of the thin air inside the AUV to heat dissipation, the external surface of the endcaps is set as an adiabatic boundary. During the simulation process, the COUPLED numerical algorithm was employed. Due to the transient nature of the high-power propulsion motor under investigation, the transient method is employed in this paper to calculate the temperature-rising process of the motor in a few minutes.

The presence of a microscopic air gap between two contacting components has been demonstrated to have a detrimental effect on the heat transfer between the components. In order to simulate the thermal behavior more accurately, the contact thermal conductance at the solid–solid interface is considered and listed in Table 4. The interface between the winding and stator core is assumed to consist of insulation paper with a thickness of 0.2 mm.

Table 4. Thermal contacting conductance between two components.

Component A	Component B	Boundary Thickness [mm]	Thermal Contact Conductance [W/m^2·K]
Winding	Stator core	0.2	1100
End winding	HBs	0.2	1100
Stator core	Motor housing	0.03	1067
Rotor core	Hub	0.03	1067
Magnets	Rotor core	0.03	1067
Machine housing	Endcap	0.03	1067
Bearing	Endcap	0.03	1067
Bearing	Shaft	0.03	1067

D.   Mesh validation

The mesh generation technique is the key to determining the computational accuracy of the FEM. In comparison to tetrahedral mesh, hexahedral mesh has a smaller number of mesh elements and a higher computational efficiency. However, their geometric adaptability is inferior. Considering the computational accuracy and the consumption of resources, a hybrid meshing method that combines hexahedral and tetrahedral meshes is employed in this paper. A hexahedral mesh is employed for the stator and rotor of the PMSM, while a tetrahedral mesh is utilized for the remaining structural components. Furthermore, in order to enhance the computational accuracy of the fluid boundary layer in contact with the solid, an inflation mesh is applied to the seawater in contact with the AUV. The aforementioned mesh generation technique is employed to generate the mesh, as shown in Figure 6.
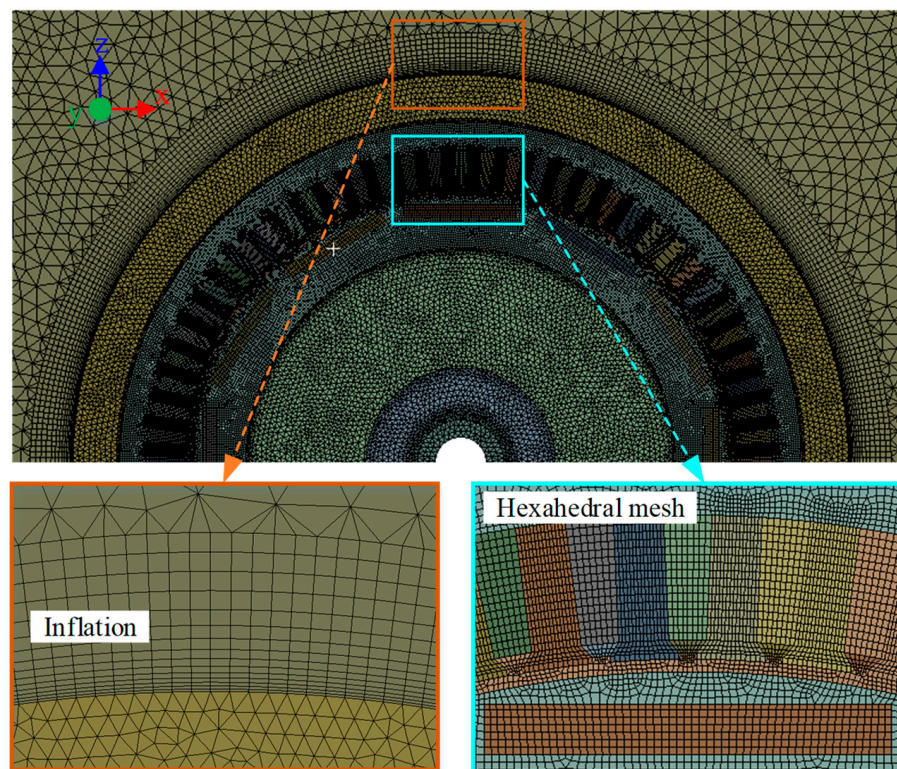
Figure 6. Mesh for the computational domain.

In order to investigate the independence of the mesh generated above, the propulsion motor is operated for 10 min at 120 kW, and the FEM is used to calculate with different quantitative scales of the mesh. The validation results of the mesh independence are shown in Table 5. The results from the 26.8 million mesh are employed as a benchmark for comparison, demonstrating that the thermal calculations for the propulsion motor remain highly consistent when the mesh increases from 18 million to 36 million. Therefore, at least 26.8 million scales of mesh are required for the subsequent calculations of the temperature rising.

Table 5. Mesh validation for the FEM.

Elements Number	Winding Temperature (K)	PMs Temperature (K)	Area-Average Heat Flux (W/m²)	Heat Flux Error (%)
18,430,136	431.56	305.84	2698.12	−0.14
21,399,341	431.50	305.85	2700.86	−0.035
26,827,263	431.42	305.84	2701.81	--
31,728,826	431.39	305.84	2702.04	0.0084
35,918,360	431.38	305.84	2707.57	0.21

Furthermore, the time-step independence of the transient calculation is also investigated with a time step of 3 to 6 s, and the corresponding results are presented in Table 6. The results show that within the 10 min transient problem investigated, time steps of 3 to 6 s have a negligible effect on the results of the thermal calculations studied. A time step of 5 s was chosen to carry out the subsequent temperature rise study in this paper.

Table 6. Time step validation for the transient FEM.

Time Steps	PMs Temperature (K)	Winding Temperature (K)	Area-Average Heat Flux (W/m^2)
3 s	305.85	431.57	2,703.13
4 s	305.85	431.54	2,701.99
5 s	305.85	431.50	2,700.86
6 s	305.85	431.47	2,699.74

3. Experimental Validation

3.1. Experimental Setup

In order to validate the electromagnetic and thermal performance of an SmPM for the AUV, a test prototype was developed and mounted on the experimental setup, as shown in Figure 7. In the test setup, DC is converted by the controller to three-phase AC and fed to the prototype motor mounted in a water tank, where the AC is measured by an oscilloscope. The mechanical energy generated by the tested prototype is measured by a torque sensor in series on the shaft and ultimately consumed by the dynamometer. During tests, the motor prototype is driven by the controller to operate at the test speed while being loaded by the dynamometer up to 120 kW or 150 kW. Three Pt100 sensors are embedded separately in the A, B, and C phase winding during the manufacturing process to monitor the temperature of the winding in real time. Considering the cost limitation of the experiment, only a section of the AUV containing the propulsion motor was developed. This results in difficulties in applying an axial high-velocity fluid on the external surface of the AUV. A section of an AUV is mounted in a tank filled with static fresh water for experimental testing. Concurrently, in order to simulate the thermal behavior of the SmPM, the inflow velocity of the seawater is set to zero when calculating the motor temperature using the FEM. The experiment was conducted at a room temperature of 28 °C and a water temperature of 15 °C. The motor windings are insulated with class H insulation, which indicates that the maximum winding temperature of the motor is not permitted to exceed 180 °C. Upon implementation of the experiment, the motor ceased operation when its temperature exceeded 170 °C.
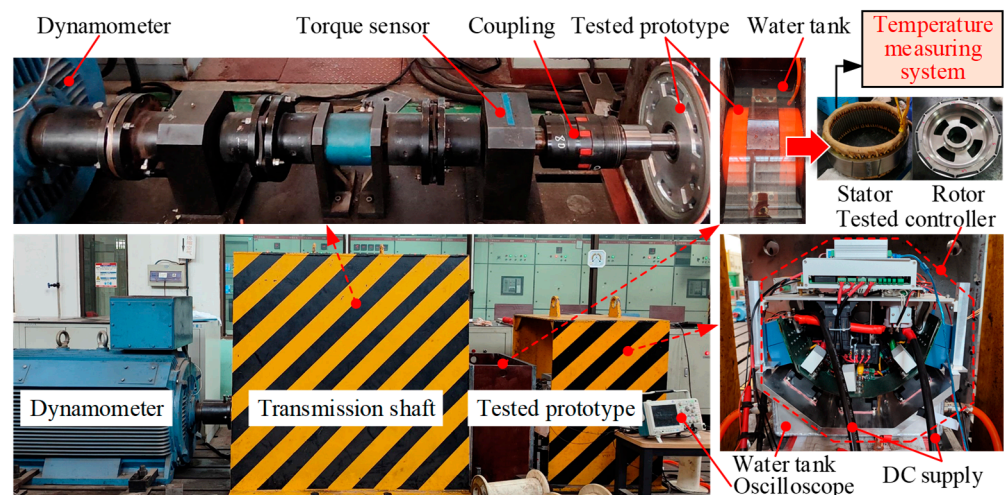
Figure 7. Simulation experiment set for the SmPM prototype.

3.2. Validation with Experimental Results

3.2.1. Electromagnetic Performance

The electromagnetic performance prediction of the motor is directly related to the accuracy of the temperature rise prediction. A Tektronix oscilloscope is used to verify the electromagnetic performance of the motor in both the no-load and 150 kW-load states.

A comparison is presented between the measured and FEM-predicted results of no-load back-EMF at speeds ranging from 500 rpm to 2500 rpm, as illustrated in Figure 8. As illustrated in Figure 8, the FEM-predicted back-EMF exhibits a high degree of agreement with the measured value. The discrepancy between the predicted and actual values is greater when the motor speed is lower, whereas the prediction accuracy improves as the speed increases. At a speed of 2500 rpm, the measured back-EMF is 229 V, while the FEM-predicted one is 230 V.
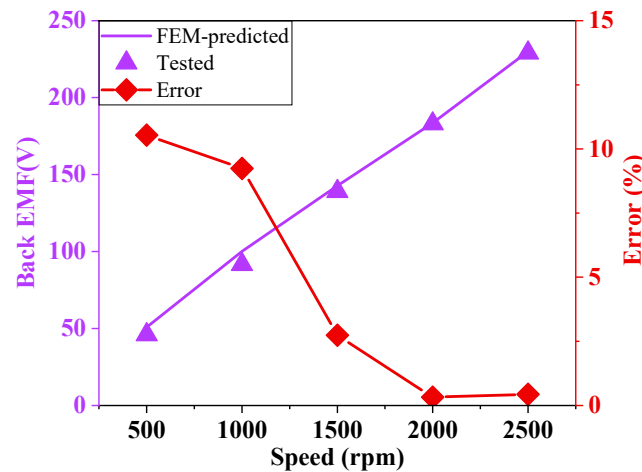
Figure 8. Comparison for the no-load back-EMF.

The loaded current waveforms of phases A and B obtained for the propulsion motor operating at 150 kW are presented in Figure 9. According to the theory of electromagnetism, the current of phase C can be predicted from the measured currents of phase A and B because the phase difference of the three-phase currents is 120° and their vector sum is zero. For a three-phase PMSM, the input power can be expressed as $P = 3UI\cos\varphi$, where U, I, and φ are the phase voltage, phase current, and their phase difference, respectively. It can be seen that the phase currents of the motor are positively correlated to the output power. Analysis of the waveforms shows that the current of phases A and B are 370 A and 372 A, respectively, while the THD is 6.9% and 9.2%, respectively. The RMS current at 150 kW is obtained using FEM as 375 A with an error of 1.3%, indicating good consistency in predicting the electromagnetic performance of the motor.
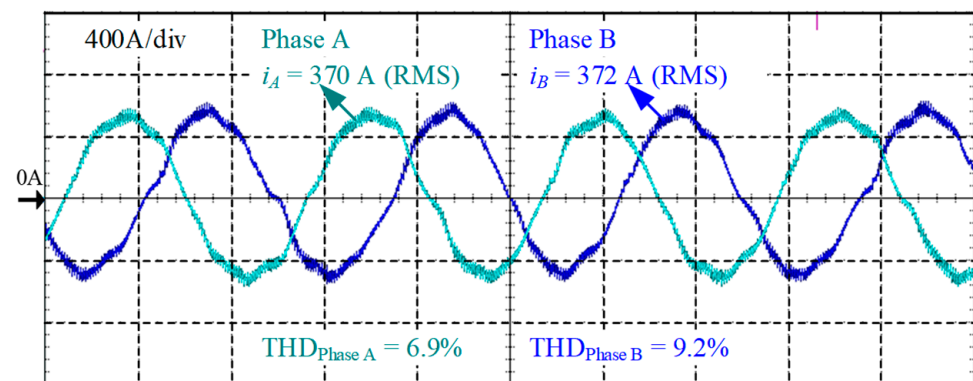

Figure 9. Current waveform when operating at 150 kW.

3.2.2. Transient Temperature Rising

The temperature rise of the winding by experimental measurement was compared with that predicted by FEM to verify the accuracy of the FEM prediction, as shown in Figure 10. It is worth noting that in the experiment, the temperature of the winding increased from room temperature to 60 °C when the output power was adjusted to 120 kW. Reasonably, the initial temperature of the winding was set to 60 °C during the numerical calculations.
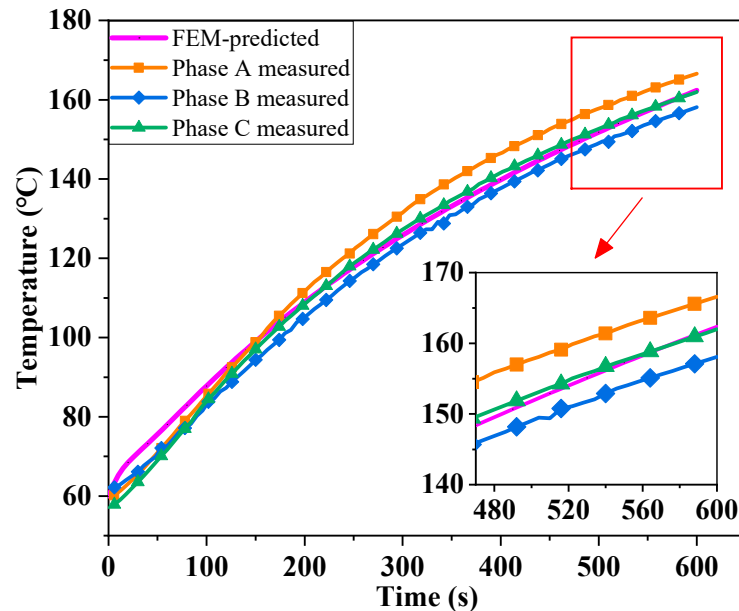

Figure 10. Comparison of real-time temperature rise.

The temperature rise process exhibits a slight imbalance in the temperature of the three-phase windings. At the 10 min moment, the highest temperature of the windings was observed in phase A at 166.4 °C, while the lowest temperature was recorded in phase B at 158.1 °C. It represents a differential temperature of 8.3 °C, which equates to a discrepancy of 5.2%. This phenomenon can be attributed to the slight imbalance in the resistance of the three-phase winding, which is a consequence of the manufacturing technique. It was observed that the temperature rise predicted by the FEM was in general agreement with that measured by the experiment. The FEM-predicted results indicate that the temperature of the winding at 10 min is approximately 162.4 °C, with a maximum difference of 4.4 °C between the measured results, implying a maximum calculation error of 2.8%. It indicates that the FEM and boundary conditions employed in this paper provide a reliable level of accuracy for the thermal prediction of the studied SmPM.

The temperature distribution contour of the motor at 120 kW for 10 min of operation was obtained by FEM calculation, as shown in Figure 11. It can be observed that the highest temperature of the stator occurs at the end of the winding, which is approximately 435.5 K. As it is being wrapped by the air with low thermal conductivity, the end winding shows localized hot spots. Moreover, the maximum temperature of the rotor is 307.9 K, which occurs on the surface of the rotor core. The 12p-72Q integer slot windings adopted in this paper exhibit a low harmonic content inside the magnetic field, resulting in low losses within the rotor.
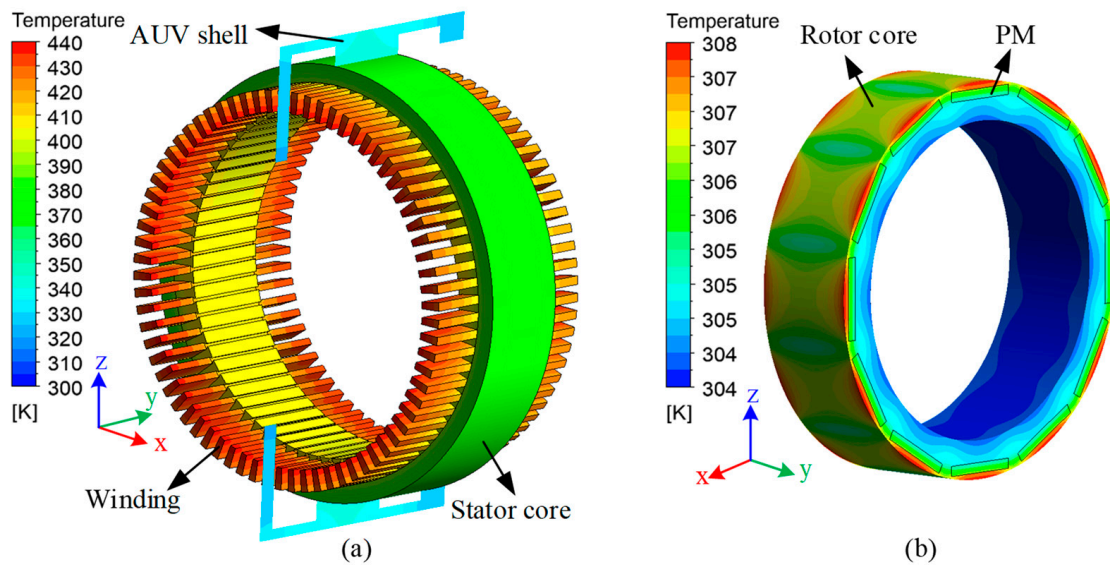
**Figure 11.** Temperature distribution contours at 10 min. (**a**) Stator. (**b**) Rotor.

4. Heat Bridges and Investigation of Thermal Effect

4.1. Heat Bridges

The temperature distribution of the motor indicates that the hottest point during operation occurs in the end winding, which is encapsulated by the hot air inside the motor. In order to suppress the temperature rising of the end winding, the U heat bridge (U-HB) and the C heat bridge (C-HB), as shown in Figure 12, are proposed and investigated in this paper. The proposed HB is constructed from a single piece of thermally conductive metal fixed to the interior surface of the AUV shell or the endcap. Simultaneously, the HB is also in contact with the external surface of the end winding, ensuring that the heat generated by the winding is effectively transferred to the AUV shell and dissipated in the seawater. Before installing the HB, the end windings of the motor should first be pressed flat with the mechanical mold. In order to reduce the thermal resistance between the HBs and the end winding, it is recommended that some thermally conductive silicone grease be coated between them. Furthermore, in consideration of the manufacturability of the HBs, it may be manufactured in pieces as illustrated in Figure 12 for facilitating mounting to the end windings.

The proposed HBs can enhance the cooling capacity of the SmPM for AUV further, resulting in a higher motor power density. Compared to propulsion motors cooled by closed oil or water jacket cooling, the scheme proposed in this paper eliminates complex piping and auxiliary equipment. It is simpler in structure and at the same time does not overburden the weight of the propulsion motor.

Due to the limited buoyancy and internal space of the AUVs, the power density of the propulsion motor is required to be as high as possible. The integrated design between the propulsion motor and the AUV shell eliminates the motor shell and adequately utilizes seawater for cooling. However, this cooling method exposes the end winding to a significant risk of overheating. In light of the aforementioned requirements, the following sections examine the potential for enhancing motor cooling through the use of the HBs, while simultaneously minimizing the additional weight. As shown in Figure 12, δ_U and δ_C represent the thickness of U-HB and C-HB, respectively, while H_U and W_C denote the height of U-HB and the width of C-HB, respectively. In the subsequent study, the propulsion motor operates at 150 kW, and the AUV sails at a speed of 21.5 m/s.
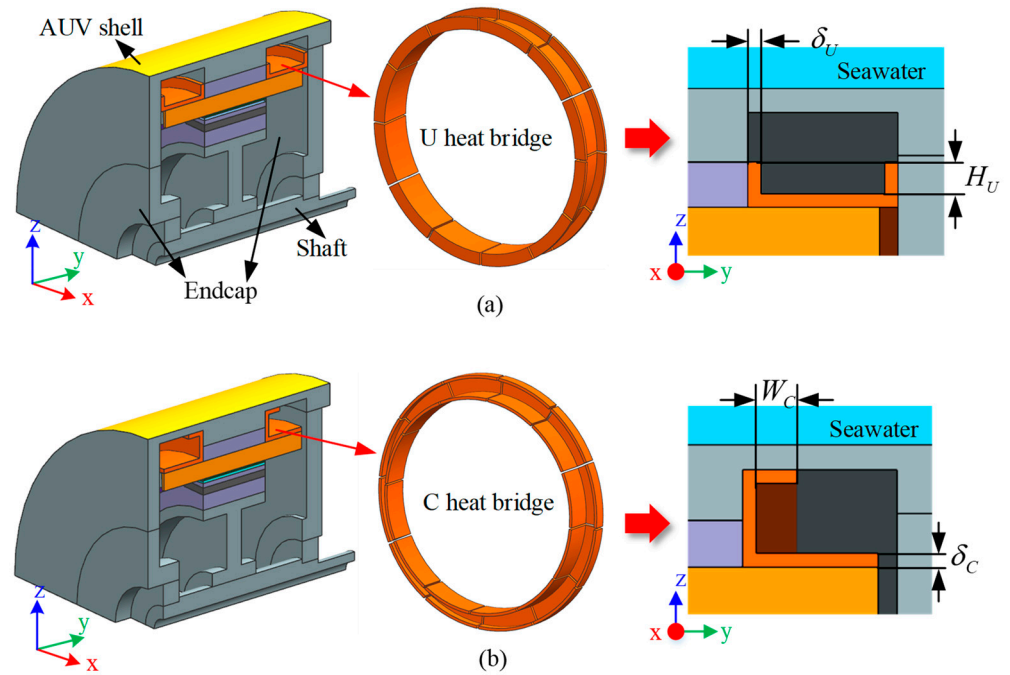
Figure 12. U heat bridge (**a**) and C heat bridge (**b**) for the SmPM.

4.2. Effect of Heat Bridges Material

Schemes with copper or aluminum alloy HBs were implemented to investigate the cooling performance of the propulsion motor and comparing to the original prototype without the HBs. The effect of the HBs' material on the maximum temperature of the winding and the heat transfer coefficient of the external surface of the AUV is shown in Figure 13. The results show that the temperature rises rapidly within a few minutes of motor start-up, while as the temperature gradient gradually increases, the cooling effect is enhanced, and the temperature growth slows down. Figure 13a illustrates that the maximum temperature of the motor after 10 min of operation at 150 kW output power decreases from 473 K in the original scheme to below 453 K with the addition of HB at the end windings. Similarly, it is observed from Figure 13b that the scheme with HBs exhibits a higher heat transfer coefficient throughout the 10 min transient. At the 10 min moment, the heat transfer coefficient of the schemes with copper C-HB and copper U-HB increased by 6.7% and 2.4%, respectively, compared to the original scheme, indicating that the C-HB is more capable of cooling than the U-HB. In comparison to U-HB, C-HB exhibits a more efficient cooling capacity. Furthermore, benefitting from the high thermal conductivity of copper, the copper HB shows a slightly better cooling effect than the aluminum alloy HB. However, it is worth noting that the density of copper is three times higher than that of aluminum alloy. Therefore, the cooling effect and the additional weight added must be taken into account when selecting the material for HBs.

The stator distribution profiles calculated for the original scheme and the schemes containing U-HB or C-HB are shown in Figure 14. It is pertinent to note that both U-HB and C-HB, which were employed as a comparison to the original scheme depicted in Figure 14, are copper HBs with $\delta_U = \delta_C = 2$ mm, $H_U = 15$ mm, and $W_C = 20$ mm. The results show that the maximum temperature at the end winding reaches 472 K following the implementation of the original scheme for a duration of 10 min at an output power of 150 kW. In contrast, the addition of U-HB or C-HB results in a reduction in the maximum temperature to 451 K or 447 K, respectively, which remain below the restrictive temperature of the insulation class. It is demonstrated that the HBs proposed in this paper are effective in reducing the temperature of the propulsion motor, thus enabling it to run at a higher output power of 150 kW for 10 min.
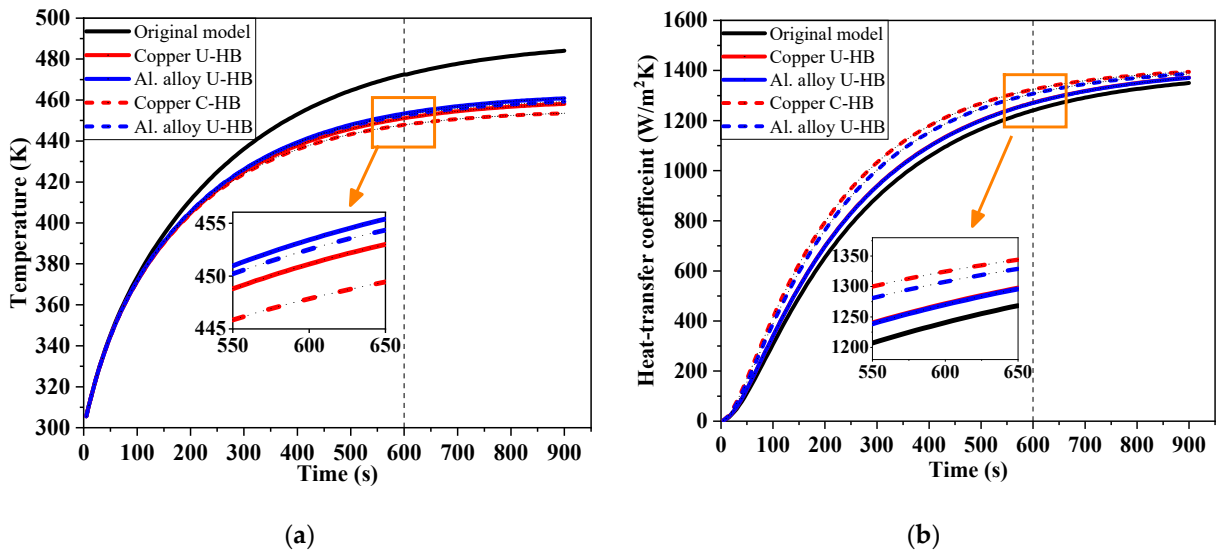
Figure 13. Effect of HB's material on temperature (**a**) and heat transfer coefficient (**b**).
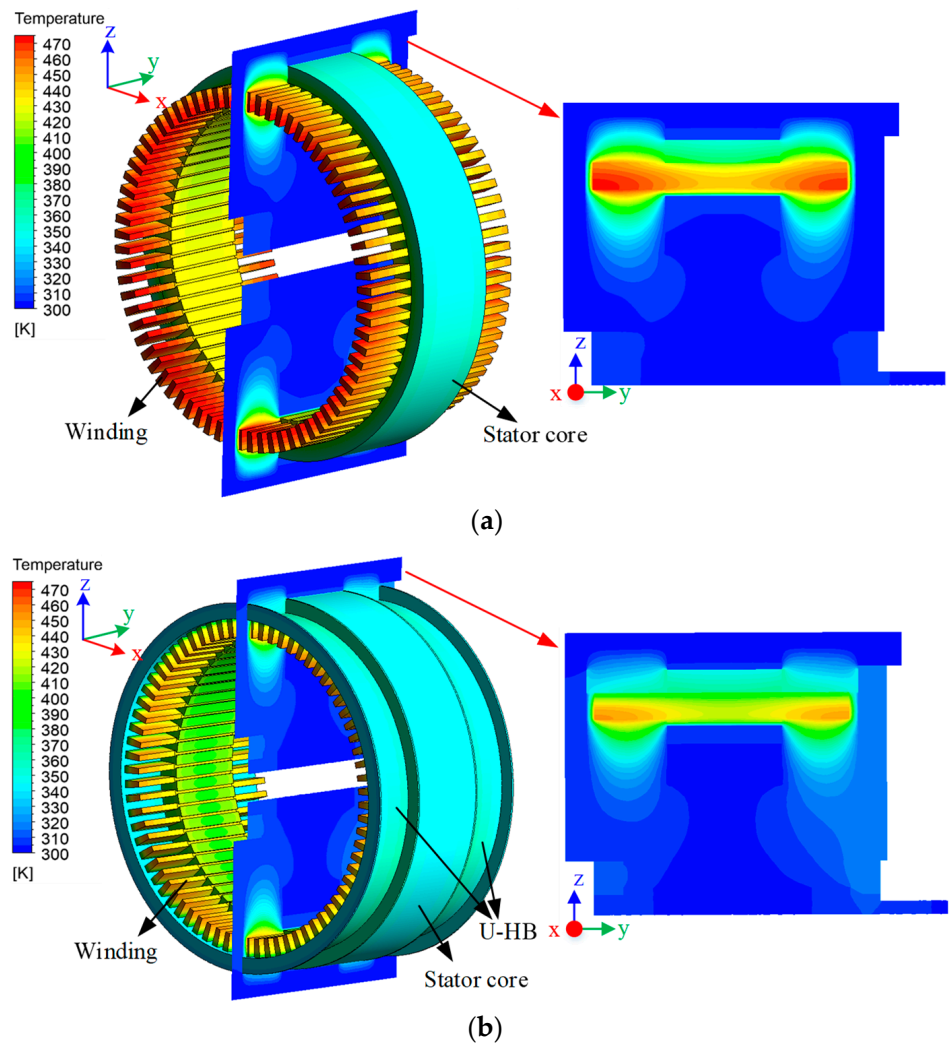

(**a**)

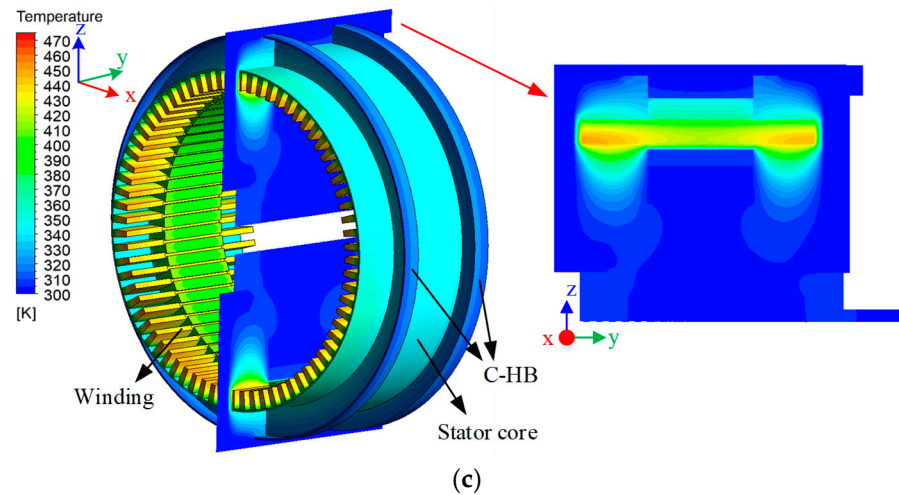

(**b**)

Figure 14. *Cont.*

(c)

Figure 14. Temperature distribution. (**a**) Initial scheme. (**b**) Scheme with U-HB. (**c**) Scheme with C-HB.

It is worth noting that since the losses in the winding are proportional to the square of the current, if the motor is running at overcurrent (overloaded), a large increase in the losses in the winding can cause the motor to overheat dramatically. In this case, the temperature in the motor should be evaluated in further detail. Fortunately, as the load on an AUV propulsion motor is related to the motor speed, which is always precisely controlled to keep the speed of the AUV under control, a sudden overload will not occur.

4.3. Effect of Geometric Dimensions

In this section, the effect of geometric dimensions on the thermal characteristics of the SmPM is investigated. As illustrated in Figure 15a, when H_U = 15 mm, an increase in the thickness of U-HB, from 1 mm to 5 mm, has been observed to result in a reduction in the maximum and average temperatures of the windings. Specifically, the maximum and average temperatures have been found to decrease from 454.2 K and 422.2 K to 448.2 K and 415.9 K, respectively. Based on the temperature rise observed at δ_U = 1 mm, it can be seen that the maximum and average temperatures have been reduced by 3.8% and 5.2%, respectively. Furthermore, an excessively thick U-HB will result in a significant increase in the weight of the propulsion motor but only a marginal improvement in the motor's cooling capacity. In the studied situation, a U-HB with δ_U = 2 mm is recommended.
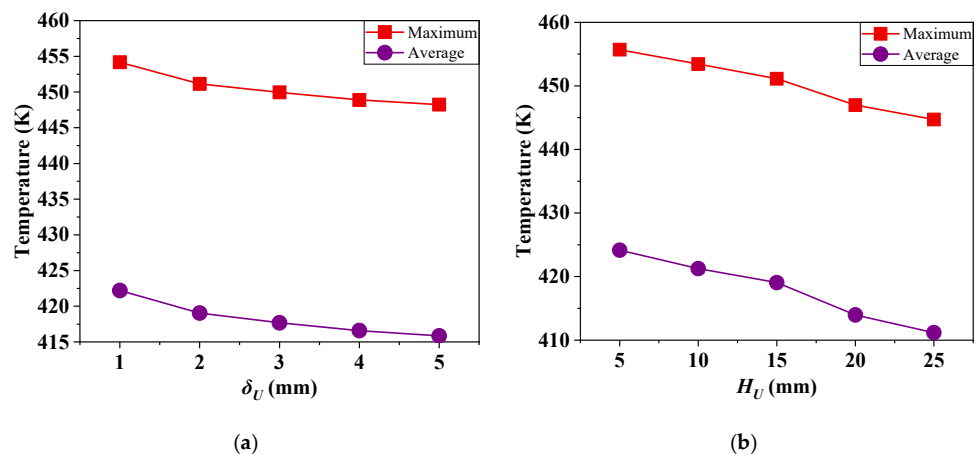

(a)　　　　　　　　　　　　**(b)**

Figure 15. Effect of geometric dimensions on thermal properties. (**a**) δ_U for U-HB. (**b**) H_U for U-HB.

On the other hand, an appropriate increase in the height of the H_U can expand the contact area of U-HB, which can effectively mitigate the temperature rise of the winding. As illustrated in Figure 15b, keeping δ_U = 2 mm, an increase in the H_U from 5 mm to

25 mm results in a reduction in the maximum and average temperatures by 11 K and 12.9 K, respectively. This indicates that the temperature rise is diminished by 7.1% and 10.4%, respectively. Consequently, as for the U-HB, it is beneficial to increase the H_U as much as possible when the weight limitations are not exceeded.

Figure 16 illustrates the impact of varying the geometry of the C-HB on the thermal characteristics of the motor. It can be observed that, in comparison to U-HB, increasing the thickness of C-HB within a certain range has a more pronounced effect on enhancing the heat dissipation capability. As shown in Figure 16a, when W_C = 20 mm, an increase in the thickness δ_C of the C-HB from 1 mm to 5 mm results in a reduction in the maximum and average temperatures of the windings by 9.9 K and 12.4 K, respectively. This represents a 6.4% and 10.2% decrease, respectively. Furthermore, an increase in the W_C from 0 mm to 40 mm when δ_C = 2 mm results in a reduction in the maximum and average temperatures of the windings by 3.2 K and 3.7 K, respectively. It can be observed that as the W_C is further increased from 20 mm, the enhancement in cooling is even more minimal. Therefore, it can be concluded that the increase in W_C is relatively limited in its ability to suppress the temperature rise for the SmPM.
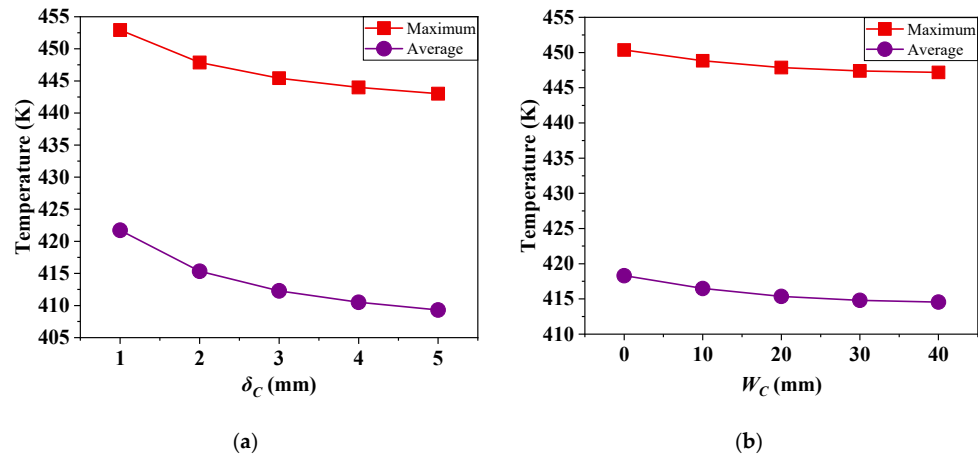

(a)

(b)

Figure 16. Effect of geometric dimensions on thermal properties. (**a**) δ_C for C-HB. (**b**) W_C for C-HB.

The comparison of the temperature suppression using U-HB and C-HB for SmPM indicates that C-HB exhibits slightly superior performance. However, it is also important to note that regardless of whether U-HB or C-HB is used, it is essential to pay close attention to the coordination between the geometry and cooling effect. Otherwise, they lose more than what one gains from HBs on SmPM.

4.4. Weight Reduction by Cooling Improvement Using HBs

As illustrated in Figure 1, the tail section of the AUV is designed to be streamlined to enhance its hydrodynamic performance. This profile makes the buoyancy of the tail section slightly weaker than that of the head section. On the other hand, the propulsion motor must be mounted in the tail section to drive the propulsor. Therefore, it is always desirable to make the propulsion motor as light as possible.

The preceding analyses have demonstrated that the winding temperature over a given time operation is effectively suppressed after increasing the HBs. On this basis, the parameters of the motor can be optimally redesigned to further reduce the weight of the motor by appropriately increasing the current density inside the winding. The scheme containing C-HB is redesigned, and the main parameters are compared before and after parameter adjustment, as shown in Table 7. In order to ensure that the magnetic field remains consistent, only the winding and the length of the stator core were redesigned, while the slot parameters of the stator and rotor were not adjusted. The results indicate that the slot fill remains largely unaltered, whereas the current density at the rated state increases from 14.55 A/mm^2 to 15.59 A/mm^2, representing an increase of 7.14%.

**Table 7.** The comparison of main parameters before and after the redesign.

Parameters	Initial Scheme	Optimized Scheme
Axial stator length [mm]	82	73
Turns	4	3
Parallel branches	3	2
Wire Gauge [mm]	1.25	1.18
Number of Strands	7	11
Slot fill	65.7%	65.3%
Current density [A/mm^2]	14.55	15.59

In the redesigned scheme, aluminum alloy C-HBs with δ_C = 2 mm and W_C = 20 mm are used. Table 8 illustrates the alteration in the weights of the stator and rotor subsequent to the redesign of the motor. Although a 1.12 kg weight burden is caused by the added HBs, the weight of the stator and rotor is reduced even more. The weight totals demonstrate that when the shell and shaft system are excluded, the weight of the electromagnetic components has been reduced by 3.29 kg, representing a 7.12% reduction.

Table 8. Weight change in electromagnetic components after parameter adjustment.

Weight [kg]	Initial Scheme	Optimized Scheme
Stator lamination	20.59	18.33
Winding	9.67	9.27
Rotor lamination	12.11	10.78
Magnet	3.84	3.42
HBs	--	1.12
Total weight	46.21	42.92

In order to verify that the optimized motor meets the temperature rise requirements at the rated state (150 kW for 6 min), the heat generation rate is recalculated, and transient thermal calculations are carried out under the same boundary conditions. The transient temperature variation is obtained and compared with the initial scheme, as displayed in Figure 17. It shows that the temperature rises of the motor before and after the optimization are essentially the same during the 6 min operation. After 6 min of operation at the rated condition, the temperatures of the windings and magnets of the optimized scheme are 435.2 K and 303.5 K respectively, which satisfy the temperature limitations. In conclusion, it is shown that the increased HBs are favorable for the further weight reduction of the SmPM.
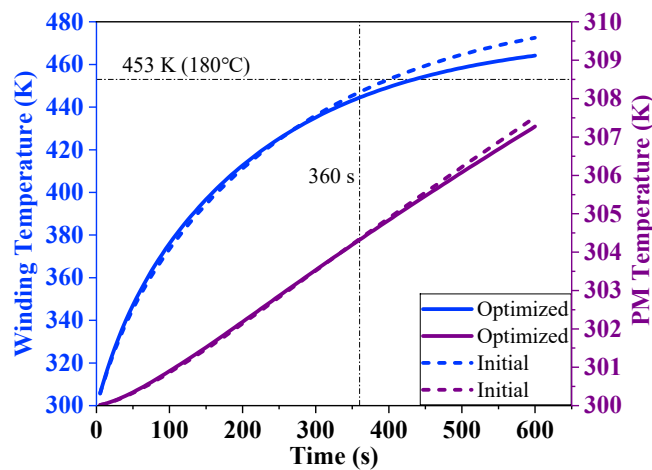
Figure 17. Change in temperature rise of the motor after optimization.

5. Conclusions

In this paper, a cooling improvement method based on HBs is proposed for the SmPM of an AUV. Based on an experimentally validated numerical method, the effects of topology, material, and geometric parameters on the cooling effect and weight reduction are investigated. The major conclusions of this paper are as follows:

(1) The FEM and boundary conditions adopted to predict the electromagnetic and thermal performance of the SmPM show good accuracy. The FEM-predicted phase current for the motor operating at 150 kW is 375 A, with a deviation of 1.3% from the experimental results. The winding temperature after 10 min operation at 120 kW was predicted by FEM to be 162.4 °C, with a deviation of 2.8% from the experimental results.

(2) Both the proposed U-HB and C-HB effectively suppress the temperature rise and improve the winding temperature consistency. The results show that after increasing the HBs proposed, a reduction of at least 20 K in the maximum winding temperature is achieved when the motor is operated at 150 kW for 10 min.

(3) A comparison of using U-HB and C-HB for the SmPM indicates that C-HB exhibits slightly superior cooling performance, and it can be improved further by optimizing the geometry. The material of HBs offers limited improvement in the cooling effect, while appropriately increasing the length and thickness of HBs can effectively enhance the cooling performance.

(4) According to the required operation time, the cooling improvement provided by HBs is conducive to the weight reduction of the SmPM. The U-HB with δ_U = 2 mm and W_C = 20 mm reduces the weight of the studied SmPM by 3.29 kg, representing a weight reduction of 7.12%.

References

1. Ridao, P.; Carreras, M.; Ribas, D.; Sanz, P.J.; Oliver, G. Intervention AUVs: The next challenge. *Annu. Rev. Control.* **2015**, *40*, 227–241. [CrossRef]
2. Wang, Z.; Luo, W.; Zhang, T.; Li, K.; Liao, Y.; Jia, J.; Jiang, D. AUV hydrodynamic coefficient offline identification based on deep reinforcement learning. *Ocean Eng.* **2024**, *304*, 117809. [CrossRef]
3. Zhang, Y.; Wang, Q.; Shen, Y.; Dai, N.; He, B. Multi-AUV cooperative control and autonomous obstacle avoidance study. *Ocean Eng.* **2024**, *304*, 117634. [CrossRef]
4. Zheng, J.; Zhao, W.; Ji, J.; Lee, C.H.T. Quantitative Analysis on Maximum Efficiency Point and Specific High-Efficiency Region of Permanent-Magnet Machines. *IEEE Trans. Ind. Electron.* **2021**, *69*, 1333–1345. [CrossRef]
5. Liu, G.; Qiu, G.; Shi, J.; Zhang, F. Study on Counter-Rotating Dual-Rotor Permanent Magnet Motor for Underwater Vehicle Propulsion. *IEEE Trans. Appl. Supercond.* **2018**, *28*, 1–5. [CrossRef]
6. Mitra, A.; Panda, J.P.; Warrior, H.V. Experimental and Numerical Investigation of the Hydrodynamic Characteristics of Autonomous Underwater Vehicles Over Sea-Beds with Complex Topography. *Ocean Eng.* **2020**, *198*, 106978. [CrossRef]
7. Li, B.; Mao, Z.; Song, B.; Wang, X.; Tian, W.; Sun, Q.; Wang, Y.-F.; Jin, Z. Experimental investigation on efficient thermal management of autonomous underwater vehicle battery packs using anisotropic expanded graphite/paraffin composite materials. *Appl. Therm. Eng.* **2024**, *242*, 122477. [CrossRef]
8. Li, B.; Mao, Z.; Song, B.; Wang, Y.-F.; Tian, W.; Lu, C.; Li, M. Performance evaluation and heat transfer mechanism for battery thermal management of autonomous underwater vehicles based on phase change material cooling. *Appl. Therm. Eng.* **2023**, *219*, 119655. [CrossRef]

9. Wang, X.; Li, B.; Gerada, D.; Huang, K.; Stone, I.; Worrall, S.; Yan, Y. A critical review on thermal management technologies for motors in electric cars. *Appl. Therm. Eng.* **2022**, *201*, 117758. [CrossRef]

10. Tikadar, A.; Johnston, D.; Kumar, N.; Joshi, Y.; Kumar, S. Comparison of electro-thermal performance of advanced cooling techniques for electric vehicle motors. *Appl. Therm. Eng.* **2020**, *183*, 116182. [CrossRef]

11. Raj, J.A.P.S.; Asirvatham, L.G.; Angeline, A.A.; Manova, S.; Rakshith, B.L.; Bose, J.R.; Mahian, O.; Wongwises, S. Thermal management strategies and power ratings of electric vehicle motors. *Renew. Sustain. Energy Rev.* **2024**, *189*, 113874. [CrossRef]

12. Chang, M.; Lai, B.; Wang, H.; Bai, J.; Mao, Z. Comprehensive efficiency analysis of air-cooled vs water-cooled electric motor for unmanned aerial vehicle. *Appl. Therm. Eng.* **2023**, *225*, 120226. [CrossRef]

13. Xu, Z.; Xu, Y.; Liu, W.; Wang, Y. Stator winding hotspot temperature rise characteristic study of an axially forced air-cooled motor with air deflector. *Appl. Therm. Eng.* **2023**, *224*, 120108. [CrossRef]

14. Li, W.; Cao, Z.; Zhang, X. Thermal Analysis of the Solid Rotor Permanent Magnet Synchronous Motors with Air-Cooled Hybrid Ventilation Systems. *IEEE Trans. Ind. Electron.* **2021**, *69*, 1146–1156. [CrossRef]

15. Na, J.S.; Ryu, C.-M.; Moon, S.J. Thermal analysis methods for wound rotor synchronous motors with water-cooling jackets. *Therm. Sci. Eng. Prog.* **2023**, *46*, 102177. [CrossRef]

16. Park, M.H.; Kim, S.C. Development and validation of lumped parameter thermal network model on rotational oil spray cooled motor for electric vehicles. *Appl. Therm. Eng.* **2023**, *225*, 120176. [CrossRef]

17. Garud, K.S.; Kang, E.-H.; Hwang, S.-G.; Lee, M.-Y. Experimental study for artificial neural network modeling on thermal and flow performances of electric traction motor with oil spray cooling. *Int. Commun. Heat Mass Transf.* **2023**, *148*, 107037. [CrossRef]

18. Lee, Y.; Choi, H.; Park, P.; Lee, H. Multi-objective optimization of a U-shaped water jacket with a guide vane for improving the thermal performance of 20 kW in-wheel motor. *Case Stud. Therm. Eng.* **2024**, *53*, 103927. [CrossRef]

19. Park, J.; Han, K.; Choi, H.-S.; Park, I.S. Cooling and dynamic performance of electric vehicle traction motor adopting direct slot cooling method. *Int. Commun. Heat Mass Transf.* **2023**, *147*, 106970. [CrossRef]

20. Garud, K.S.; Hwang, S.-G.; Han, J.-W.; Lee, M.-Y. Performance characteristics of the direct spray oil cooling system for a driving motor of an electric vehicle. *Int. J. Heat Mass Transf.* **2022**, *196*, 123228. [CrossRef]

21. Garud, K.S.; Lee, M.-Y. Thermal management characteristics of electric vehicle driving motor with oil spray cooling based on spray locations and oil types. *Appl. Therm. Eng.* **2024**, *248*, 123234. [CrossRef]

22. Wang, H.; Liu, X.; Kang, M.; Guo, L.; Li, X. Oil Injection Cooling Design for the IPMSM Applied in Electric Vehicles. *IEEE Trans. Transp. Electrification* **2022**, *8*, 3427–3440. [CrossRef]

23. Dutta, R.; Pouramin, A.; Rahman, M.F. A Novel Rotor Topology for High-Performance Fractional Slot Concentrated Winding Interior Permanent Magnet Machine. *IEEE Trans. Energy Convers.* **2021**, *36*, 658–670. [CrossRef]

24. Thike, R.; Pillay, P. Mathematical Model of an Interior PMSM With Aligned Magnet and Reluctance Torques. *IEEE Trans. Transp. Electrification* **2020**, *6*, 647–658. [CrossRef]

25. Wojda, R.; Kazimierczuk, M. Winding resistance of litz-wire and multi-strand inductors. *IET Power Electron.* **2012**, *5*, 257–268. [CrossRef]

26. Wrobel, R.; Salt, D.E.; Griffo, A.; Simpson, N.; Mellor, P.H. Derivation and Scaling of AC Copper Loss in Thermal Modeling of Electrical Machines. *IEEE Trans. Ind. Electron.* **2013**, *61*, 4412–4420. [CrossRef]

27. Tong, W.; Li, S.; Sun, R.; Sun, L.; Tang, R. Modified Core Loss Calculation for High-Speed PMSMs With Amorphous Metal Stator Cores. *IEEE Trans. Energy Convers.* **2020**, *36*, 560–569. [CrossRef]

28. Zhu, L.; Fan, B.; Han, X.; Tang, R. Effects of shrink fitting on iron losses of a permanent magnet synchronous motor with an amorphous core. *IET Electr. Power Appl.* **2022**, *16*, 996–1003. [CrossRef]

29. Bertotti, G. General properties of power losses in soft ferromagnetic materials. *IEEE Trans. Magn.* **1988**, *24*, 621–630. [CrossRef]

30. Chang, L.; Jahns, T.M.; Blissenbach, R. Generalized Dynamic Hysteresis Model for Improved Iron Loss Estimation of Complex Flux Waveforms. *IEEE Trans. Magn.* **2019**, *55*, 2889239. [CrossRef]

31. Zhu, Q.; Wu, Q.; Li, W.; Pham, M.-T.; Zhu, L. A General and Accurate Iron Loss Calculation Method Considering Harmonics Based on Loss Surface Hysteresis Model and Finite-Element Method. *IEEE Trans. Ind. Appl.* **2020**, *57*, 374–381. [CrossRef]

32. Yamazaki, K.; Fukushima, Y. Effect of Eddy-Current Loss Reduction by Magnet Segmentation in Synchronous Motors with Concentrated Windings. *IEEE Trans. Ind. Appl.* **2011**, *47*, 779–788. [CrossRef]

33. Menter, F.R. Review of the shear-stress transport turbulence model experience from an industrial perspective. *Int. J. Comput. Fluid Dyn.* **2009**, *23*, 305–316. [CrossRef]

34. Menter, F.R. Two-equation eddy-viscosity turbulence models for engineering applications. *AIAA J.* **1994**, *32*, 1598–1605. [CrossRef]

35. Liu, J.; Ai, M. Structural optimization design and heat transfer characteristics of air-to-air cooled high voltage motor heat exchanger. *Case Stud. Therm. Eng.* **2022**, *40*, 102532. [CrossRef]

36. Jaritz, M.; Hillers, A.; Biela, J. General Analytical Model for the Thermal Resistance of Windings Made of Solid or Litz Wire. *IEEE Trans. Power Electron.* **2018**, *34*, 668–684. [CrossRef]

37. Boglietti, A.; Cavagnino, A.; Staton, D.; Shanel, M.; Mueller, M.; Mejuto, C. Evolution and Modern Approaches for Thermal Analysis of Electrical Machines. *IEEE Trans. Ind. Electron.* **2009**, *56*, 871–882. [CrossRef]

38. Simpson, N.; Wrobel, R.; Mellor, P.H. Estimation of Equivalent Thermal Parameters of Impregnated Electrical Windings. *IEEE Trans. Ind. Appl.* **2013**, *49*, 2505–2515. [CrossRef]

39. Boglietti, A.; Carpaneto, E.; Cossale, M.; Vaschetto, S. Stator-Winding Thermal Models for Short-Time Thermal Transients: Definition and Validation. *IEEE Trans. Ind. Electron.* **2015**, *63*, 2713–2721. [CrossRef]